

# Material Decomposition in Photon-Counting Computed Tomography with Diffusion Models: Comparative Study and Hybridization with Variational Regularizers

Corentin Vazia, Thore Dassow, Alexandre Bousse, Jacques Froment, Béatrice Vedel, Franck Vermet, Alessandro Perelli, Jean-Pierre Tasu and Dimitris Visvikis

**Abstract**—Photon-counting computed tomography (PCCT) has emerged as a promising imaging technique, enabling spectral imaging and material decomposition (MD). However, images typically suffer from a low signal-to-noise ratio due to constraints such as low photon counts and sparse-view settings which provoke artifacts. To prevent this, variational methods minimize a data-fit function coupled with handcrafted regularizers which mimics a prior by enforcing image properties such as the sparsity of the gradient. In the last few years, diffusion models (DMs) became predominant in the field of generative models and have been used as a learned prior for image reconstruction. This work investigates the use of DMs as regularizers for MD tasks in PCCT, specifically using diffusion posterior sampling (DPS) guidance. Three DPS-based approaches—image-domain two-step DPS (im-TDPS), projection-domain two-step DPS (proj-TDPS), and one-step DPS (ODPS)—are evaluated. The first two methods perform MD in two steps by performing reconstruction and MD separately. The last method, ODPS, samples the material images directly from the measurement data. The results indicate that ODPS achieves superior performance compared to im-TDPS and proj-TDPS, providing sharper, noise-free and crosstalk-free images. Furthermore, we introduce a novel hybrid ODPS method for scenarios involving materials absent from the training dataset. This methods combine DM priors with standard variational handcrafted regularizers for the materials unknown to the DM. This hybrid method demonstrates improved MD quality compared to a standard variational method and does not require additional training of the DM neural network (NN).

**Index Terms**—Diffusion Posterior Sampling (DPS), Photon-Counting Computed Tomography (PCCT), Material Decomposition (MD)

C. Vazia and T. Dassow share first authorship.

This work involved human subjects or animals in its research. The author(s) confirm(s) that all human/animal subject research procedures and protocols are exempt from review board approval.

This work was supported by the French National Research Agency (ANR) under grant No ANR-20-CE45-0020, by France Life Imaging under grant No ANR-11-INBS-0006, by CPER 2021–2027 IMAGIIS (INNOV-XS) and by the Royal Academy of Engineering under the RAEng / Leverhulme Trust Research Fellowship LTRF-2324-20-160.

C. Vazia, J. Froment and B. Vedel are with Univ Bretagne Sud, CNRS 6205, LMBA, F-56000 Vannes, France.

T. Dassow, A. Bousse and D. Visvikis are with Univ. Brest, LaTIM, Inserm, U1101, 29238 Brest, France.

Franck Vermet is with Univ. Brest, CNRS 6205, LMBA, 29000 Brest, France.

T. Dassow is also with Siemens Healthcare SAS, Courbevoie, France.

A. Perelli is with University of Dundee, Dundee, UK.

J.-P. Tasu is with Department of Radiology, University Hospital Poitiers, Poitiers, France.

Corresponding authors: bousse@univ-brest.fr.

## I. INTRODUCTION

**X**-RAY computed tomography (CT), primarily used for medical applications, produces monochromatic linear attenuation coefficients (LAC) images without considering the full energy spectrum of the crossing beam. However, in the last decade, photon-counting computed tomography (PCCT) [1], and more generally spectral CT, have enabled the consideration of the energy of the X-ray spectrum [2]. This advancement allows for polychromatic imaging with energy-dependent LAC. However, in spectral CT, measurements are grouped into energy bins that have a lower source intensity compared to classical CT. Furthermore, due to public health concerns, efforts must be made to reduce radiation exposure “as low as reasonably achievable”. This can be accomplished either by reducing the photon count per projection (low count) or by lowering the number of projection angles (sparse view). This leads to a low signal-to-noise ratio in each energy bin and potential streak artifacts in the reconstructed images, and therefore spectral CT image reconstruction requires regularization. Synergistic regularization is a way to leverage the structural similarities between the spectral images. Such regularizations include handcrafted regularizers [3] as well as learned regularizers [4], [5].

Using the energy dependence of the LACs, material decomposition (MD) can be performed [6]. This approach enables the generation of material-specific maps, such as bones, soft tissues, or iodine tracers. MD can provide insight into atherosclerotic plaque composition [7], classifies renal stones [8]–[10], improves lesion detection and characterization [11], and offers a wide range of clinical applications [12]. However, MD is contingent on image reconstruction and therefore requires regularization. This can be achieved through a maximization *a posteriori* (MAP) formulation with a handcrafted or a learned prior. Methods addressing the MD problem typically fall into one of two categories: (i) one-step methods, where reconstruction and decomposition are performed simultaneously [13], [14], making the problem non-convex and highly ill-posed; or (ii) two-step methods [15]–[18], where each subproblem is solved sequentially. Section II-B provides an overview of the main approaches to MD formulation.

In recent years, artificial intelligence (AI)-based approaches have become state-of-the-art for image and text generation

[19]–[21] and for solving inverse problems such as image reconstruction [22] and more particularly in spectral CT [2], [23], [24]. Among them, diffusion models (DMs) have shown promising results [25]–[28], particularly in medical image reconstruction [29]. In high dimensions, using diffusion posterior sampling (DPS) is usually computationally more feasible than other DM based methods. In a recent work, we proposed to use DM through DPS as a synergistic regularizer for spectral CT image reconstruction [30]. More recently, Jiang *et al.* [31] used a DPS framework for one-step MD in dual-energy CT. At the same time, we independently proposed a similar one-step MD framework for PCCT [32].

In this paper, we investigate multiple ways of incorporating diffusion prior into the MD problem. We evaluate three DPS-based MD approaches in a PCCT setting, including two two-step DPS approaches, namely image-domain two-step DPS (im-TDPS) and projection-domain two-step DPS (proj-TDPS), and a one-step DPS (ODPS) approach. Dual image/material DM-based priors were not considered as they are too computationally expensive. In addition, we only considered image domain priors (either on material or spectral images) so that the neural networks (NNs) are not impacted by potential changes on the projection geometry such as the number of projection angles. We compared these methods with other state-of-the-art techniques in two low-dose settings (full-view and sparse-view).

In addition, we propose a new method consisting of mixing the diffusion prior with standard variational regularizers, which can be utilized in situations where some of the material maps are not present in the training database. For such materials, a pseudo-prior, derived from the variational regularization of inverse problems, is combined with the DM-learned prior. This variational regularizer is chosen interdependently of the DM and incorporated in a single line of the algorithm. Therefore, this hybrid-ODPS heuristic retains the powerful regularization of the DM while incorporating new materials such as iodine, providing a potential solution for real-world clinical and research scenarios and avoiding retraining.

The remainder of the paper is structured as follows. We first present the MD problem in PCCT in Section II, including the two-step and one-step paradigms. Then, Section III reviews the DPS method to regularize this inverse problem and introduces our hybridization method with variational regularizers. Section IV shows the data used for the experiments. After a description of the methods used for comparison, we present and discuss the obtained results. Section V discusses the proposed methods and present perspectives for future works. Finally, Section VI concludes this work.

### Notations

The superscripts ‘ $\top$ ’ and ‘ $\dagger$ ’ respectively denote the matrix transposition and Moore-Penrose inverse.

Given a real-valued matrix  $\mathbf{c} = \{c_{n,m}\}_{n,m=1}^{N,M} \in \mathbb{R}^{N \times M}$ ,  $\mathbf{c}_{n,:}$  and  $\mathbf{c}_{:,m}$  respectively denotes the  $n$ -th row and  $m$ -th column of  $\mathbf{c}$ , i.e.,

$$\mathbf{c}_{n,:} = [c_{n,1}, \dots, c_{n,M}], \quad \mathbf{c}_{:,m} = [c_{1,m}, \dots, c_{N,m}]^\top.$$

For a given real-valued vector  $\mathbf{c} = \{c_n\}_{n=1}^N \in \mathbb{R}^N$ ,  $[\mathbf{c}]_n$  denotes the  $n$ -th entry of  $\mathbf{c}$ , i.e.,  $[\mathbf{c}]_n = c_n$ . The zero element

and the identity matrices (with dimensions given by the context) are denoted  $\mathbf{0}$  and  $\mathbf{I}$ , respectively. Capital letters represent random vectors, and their lowercase equivalent represents their realization. For example, for a given pair  $(\mathbf{X}, \mathbf{Y})$  of random vectors,  $p_{\mathbf{X}|\mathbf{Y}=\mathbf{y}}(\mathbf{x})$  represents the conditional probability distribution function (PDF) of  $\mathbf{X}$  evaluated at  $\mathbf{x}$  given  $\mathbf{Y} = \mathbf{y}$ . Bold calligraphic capital letters represent vector-valued operators.

## II. BACKGROUND ON MATERIAL DECOMPOSITION

This section presents the forward measurement model and presents the three (non AI-based) main approaches for material decomposition.

### A. Measurement Model

We assume that the imaged object is a vector sampled on a grid composed of  $n_p$  pixels. The X-ray attenuation image takes the form of an energy-dependent random column vector  $\mathbf{U}(e)$ ,

$$\mathbf{U}(e) = [U_1(e), \dots, U_{n_p}(e)]^\top$$

where  $U_j(e)$  is the LAC at pixel location  $j$  and for an incoming beam of energy  $e \in \mathbb{R}_+^*$ .

The attenuation  $\mathbf{U}$  is determined by the  $n_m$  materials that compose the object. For all pixels  $j = 1, \dots, n_p$  and materials  $m = 1, \dots, n_m$ , let us denote by  $Z_{j,m}$  the concentration of material  $m$  in the pixel  $j$ , and by  $\mathbf{Z} = \{Z_{j,m}\}_{j,m=1}^{n_p, n_m}$  the  $n_m$  channel material image, which takes the form of a  $n_p \times n_m$  random matrix;  $\mathbf{Z}_{:,m}$  corresponds the  $m$ -th material image and  $\mathbf{Z}_{j,:}$  is the vector of materials in pixel  $j$ .

The relationship between  $U_j$  and  $\mathbf{Z}_{j,:}$  is given by the energy-dependent mapping  $\mathcal{F}(\cdot, e): \mathbb{R}^{n_m} \rightarrow \mathbb{R}$  as

$$\begin{aligned} U_j(e) &= \sum_{m=1}^{n_m} f_m(e) Z_{j,m} \\ &:= \mathcal{F}(\mathbf{Z}_{j,:}, e) \end{aligned}$$

where  $f_m(e)$  is the X-ray mass attenuation coefficient of material  $m$  at energy  $e$ . Furthermore,  $\mathcal{F}$  can be generalized to a vector valued application  $\mathcal{F}$  of the entire material image  $\mathbf{Z}$  and the energy  $e$  as

$$\begin{aligned} \mathcal{F}(\mathbf{Z}, e) &:= [\mathcal{F}(\mathbf{Z}_{1,:}, e), \dots, \mathcal{F}(\mathbf{Z}_{n_p,:}, e)]^\top \\ &= \mathbf{U}(e). \end{aligned}$$

In PCCT, the measurement represents the number of X-ray photons detected along each beam, categorized into energy bins. Let  $n_b = n_\theta \cdot n_d$  denote the total number of beams, where  $n_\theta$  is the number of projection angles, and  $n_d$  is the number of detectors. Furthermore, let  $n_e$  represent the number of energy bins, with each bin corresponding to an energy interval  $[e_{k-1}, e_k]$ ,  $k = 1, \dots, n_e$ . Given a realization  $\mathbf{z} \in \mathbb{R}^{n_p \times n_m}$  of  $\mathbf{Z}$ , the number of detected photons along the  $i$ -th ray,  $i = 1, \dots, n_b$ , and in energy bin  $k$  is modeled by a random variable  $Y_{i,k}$  with conditional distribution

$$(Y_{i,k} | \mathbf{Z} = \mathbf{z}) \sim \text{Poisson}(\bar{y}_{i,k}(\mathbf{z})). \quad (1)$$

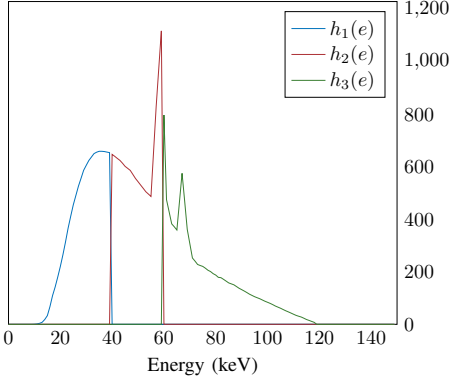


Fig. 1: Binned X-ray energy spectrum, with  $n_e = 3$  energy bins, that we used in our simulations.

The expected number of counts  $\bar{y}_{i,k}(\mathbf{z})$  is given by applying the Beer-Lambert law to  $\mathbf{U}(e) = \mathcal{F}(\mathbf{z}, e)$  and integrating in energy, i.e.,

$$\begin{aligned} \bar{y}_{i,k}(\mathbf{z}) &:= \int_0^{+\infty} h_k(e) \cdot e^{-[\mathcal{A}(\mathcal{F}(\mathbf{z}, e))]_i} de \\ &= \mathbb{E}[Y_{i,k} \mid \mathbf{Z} = \mathbf{z}] \end{aligned} \quad (2)$$

where  $\mathcal{A}: \mathbb{R}^{n_p} \rightarrow \mathbb{R}^{n_b}$  is the operator that computes the line integrals along each of the  $n_b$  X-ray beams and  $h_k(e)$  is the photon flux for the energy bin  $k$  (see Figure 1). Finally, we denote by  $\mathbf{Y} = \{Y_{i,k}\}_{i,k=1}^{n_b, n_e}$  the entire measurement vector. Note that since the relationship between  $\mathbf{Z}$  and  $\mathbf{U}$  is deterministic, conditioning  $\mathbf{Y}$  on  $\mathbf{Z}$  or  $\mathbf{U}$  is equivalent, i.e., they are equal in distribution,

$$\mathbf{Y} \mid \mathbf{Z} \sim \mathbf{Y} \mid \mathbf{U}.$$

Moreover, the random variables  $Y_{i,k}$  are conditionally independent given  $\mathbf{U}$ .

### B. Material Decomposition

MD is the task of finding an estimate  $\hat{\mathbf{z}} \in \mathbb{R}^{n_p \times n_m}$  of  $\mathbf{Z}$  given a realization  $y$  of the random variable  $\mathbf{Y}$ . We summarize the three main approaches from the literature, starting from the two-step approaches and then the one-step approach.

1) *Image-domain Material Decomposition*: This MD approach finds an estimate  $\hat{\mathbf{z}}$  in a two-step process, i.e.,

$$\hat{\mathbf{u}} \in \arg \max_{\mathbf{u}} p_{\mathbf{Y} \mid \mathbf{U}=\mathbf{u}}(\mathbf{y}) \cdot p_{\mathbf{U}}(\mathbf{u}) \quad (3)$$

$$\text{then finding } \hat{\mathbf{z}} \text{ s.t. } \mathcal{F}(\hat{\mathbf{z}}, \cdot) = \hat{\mathbf{u}}(\cdot).$$

However solving the MAP problem (3) with respect to a continuous function of the energy  $\mathbf{u}(e)$  is challenging and a common practice for this approach is to utilize an energy-discretized version of  $\mathbf{U}$ , i.e.,

$$\mathbf{X} = [\mathbf{X}_1, \dots, \mathbf{X}_{n_e}], \quad \mathbf{X}_k = \mathbf{U}(\bar{e}_k) \quad \forall k \in \{1, 2, \dots, n_e\}$$

where  $\bar{e}_k$  is the weighted mean of the photon flux for the  $k$ -th bin. Thus, the following approximated forward model can be used:

$$\begin{aligned} \mathbf{x} &= \mathcal{F}_{\text{discr}}(\mathbf{z}), \quad \bar{y}_{i,k}(\mathbf{x}_k) \approx \bar{h}_k \cdot e^{-[\mathcal{A}(\mathbf{x}_k)]_i}, \\ (Y_{i,k} \mid \mathbf{X}_k = \mathbf{x}_k) &\sim \text{Poisson}(\bar{y}_{i,k}(\mathbf{x}_k)) \end{aligned} \quad (4)$$

where  $\bar{h}_k := \int h_k(e) de$  is the total photon flux at bin  $k$  and

$$\begin{aligned} \mathcal{F}_{\text{discr}}: \mathbb{R}^{n_p \times n_m} &\rightarrow \mathbb{R}^{n_p \times n_e} \\ \mathbf{z} &\mapsto [\mathcal{F}(\mathbf{z}, \bar{e}_1), \dots, \mathcal{F}(\mathbf{z}, \bar{e}_{n_e})] \end{aligned}$$

is the discretized version of  $\mathcal{F}$ . The two-step MAP estimation therefore simplifies to

$$\hat{\mathbf{x}} \in \arg \max_{\mathbf{x}} p_{\mathbf{Y} \mid \mathbf{X}=\mathbf{x}}(\mathbf{y}) \cdot p_{\mathbf{X}}(\mathbf{x}) \quad (5)$$

$$\text{then finding } \hat{\mathbf{z}} \text{ s.t. } \mathcal{F}_{\text{discr}}(\hat{\mathbf{z}}) = \hat{\mathbf{x}}. \quad (6)$$

The conditional PDF  $p_{\mathbf{Y} \mid \mathbf{X}}$  is given by (1) and the approximate model (4). The joint PDF  $p_{\mathbf{X}} = p_{\mathbf{X}_1, \dots, \mathbf{X}_{n_e}}$  is unknown but can be replaced with synergistic regularizers. As an example of such regularizers, total nuclear variation [3] promotes structural similarities across channels or with a reference image [33]. Trained regularizers include multichannel dictionary learning (DiL) approaches such as with tensor DiL [34], convolutional DiL [5], or U-Nets [24]. Similarly, MD sub-problem (6) can be solved with DiL [15].

2) *Projection-domain Material Decomposition*: The operators  $\mathcal{F}$  and  $\mathcal{A}$  can be interchanged so that the forward model (2) can be defined through the material sinograms. More precisely, given a material image  $\mathbf{Z}$  and the corresponding material sinograms  $\mathbf{L} = [\mathcal{A}(\mathbf{Z}_{:,1}), \dots, \mathcal{A}(\mathbf{Z}_{:,n_m})]$ , we have

$$\begin{aligned} (Y_{i,k} \mid \mathbf{Z} = \mathbf{z}) &\sim (Y_{i,k} \mid \mathbf{L} = \ell) \\ &\sim \text{Poisson}(\bar{y}_{i,k}(\ell_{i,:})) \end{aligned}$$

with

$$\bar{y}_{i,k}(\ell_{i,:}) = \int_0^{+\infty} h_k(e) \cdot e^{-\mathcal{F}(\ell_{i,:}, e)} de.$$

Projection-domain MD consists in first finding an estimate  $\hat{\ell}$  of  $\ell$  (projection-based MD step) followed by deriving  $\hat{\mathbf{z}}$  from  $\hat{\ell}$  (material reconstruction step):

$$\hat{\ell} \in \arg \max_{\ell} p_{\mathbf{Y} \mid \mathbf{L}=\ell}(\mathbf{y}) \quad (7)$$

$$\text{then finding } \hat{\mathbf{z}} \text{ s.t. } \mathcal{A}_{\text{mat}}(\hat{\mathbf{z}}) \approx \hat{\ell} \quad (8)$$

where  $\mathcal{A}_{\text{mat}}: \mathbb{R}^{n_p \times n_m} \rightarrow \mathbb{R}^{n_b} \times \mathbb{R}^{n_m}$  is the material projector defined as

$$\mathcal{A}_{\text{mat}}(\mathbf{z}) := [\mathcal{A}(\mathbf{z}_{:,1}), \dots, \mathcal{A}(\mathbf{z}_{:,n_m})].$$

Note that solving (7) does not involve a prior PDF for  $\mathbf{L}$  although a regularization can be added [17].

In order to use the DPS method (Section III-A2), we need to formulate (8) in a MAP fashion. This requires us to assume that the relationship between  $\mathbf{Z}$  and  $\mathbf{L}$  is not deterministic. We choose the following inference model:

$$(\mathbf{L} \mid \mathbf{Z} = \mathbf{z}) \sim \mathcal{N}(\mathcal{A}_{\text{mat}}(\mathbf{z}), \sigma^2 \mathbf{I}). \quad (9)$$

The resulting MAP estimation for  $\mathbf{z}$  is

$$\hat{\mathbf{z}} = \arg \max_{\mathbf{z}} p_{\mathbf{L} \mid \mathbf{Z}=\mathbf{z}}(\hat{\ell}) \cdot p_{\mathbf{Z}}(\mathbf{z}) \quad (10)$$

where  $\hat{\ell}$  is a solution of (7) and the parameter  $\sigma$  in (9) gives the weight of  $p_{\mathbf{L} \mid \mathbf{Z}=\mathbf{z}}$ .

3) *One-step Material Decomposition*: This MD approach consists in finding an estimate  $\hat{\mathbf{z}}$  by solving a single problem that combines decomposition and reconstruction, generally derived from a MAP estimation, i.e.,

$$\hat{\mathbf{z}} \in \arg \max_{\mathbf{z}} p_{\mathbf{Y}|\mathbf{Z}=\mathbf{z}}(\mathbf{y}) \cdot p_{\mathbf{Z}}(\mathbf{z}). \quad (11)$$

The conditional PDF  $p_{\mathbf{Y}|\mathbf{Z}=\mathbf{z}}(\mathbf{y})$  corresponds to the data-fidelity term and is derived from (1) and (2) while the prior PDF is unknown and is generally replaced by a regularizer that promotes piecewise smooth images [13]. Solving (11) is achieved with the help of iterative algorithms such as optimization transfer [13] or limited-memory Broyden-Fletcher-Goldfarb-Shanno (L-BFGS) [35], [36]—which we used in this work.

### C. Summary of the Methods

Two-step MD approaches solve sequentially the tomographic reconstruction problem and the MD problem. Image-domain MD relies on an approximation (4) for step (5), which assumes that the energy spectrum is a weighted sum of Dirac functions in each energy bin  $k$ . This results in MD errors in step (6), such as crosstalks between the materials. Projection-domain MD does not use this approximation in step (7) but the final material imaged obtained in step (8) is not a MAP estimate given the measurement  $\mathbf{Y} = \mathbf{y}$ . On the other hand, one-step MD (11) is an actual MAP given the measurement and is known to outperform image-domain and projection-domain MD [14], [37].

## III. PROPOSED METHOD: MATERIAL DECOMPOSITION BY DIFFUSION POSTERIOR SAMPLING

DMs [19], [20] are the new state-of-the-art generative models for solving inverse problems [25] and particularly in medical image reconstruction [29]. This section shows how to incorporate DMs to the three MD approaches discussed in Section II-B.

In previous work [30] we proposed a two-step DPS MD framework consisting of (i) sampling the multi-energy image  $\mathbf{X} = [\mathbf{X}_1, \dots, \mathbf{X}_{n_e}]$  by DPS using a DM-trained prior  $p_{\mathbf{x}}(\mathbf{X})$  in the multi-energy image domain and guided by the approximated log-posterior gradient  $\nabla_{\mathbf{x}} \log p_{\mathbf{Y}|\mathbf{X}=\mathbf{x}}(\mathbf{y})$  given by (4), followed by (ii) estimating the material image  $\mathbf{z}$  by solving (6). This method is the DPS analogue of (5) and (6) and is referred to as im-TDPS.

Another approach, which we evaluate in this paper, consists of sampling  $\mathbf{Z}$  using a DM-trained prior  $p_{\mathbf{z}}$  on the material image domain and guided by the pseudo log-posterior  $\nabla_{\mathbf{z}} \log p_{\mathbf{L}|\mathbf{Z}=\mathbf{z}}(\hat{\ell})$  given by (9) where the estimated projected materials  $\hat{\ell}$  are obtained by solving (7). This method is the analogue of (10) and is referred to as proj-TDPS.

Alternatively,  $\mathbf{Z}$  can be directly sampled by DPS from the data  $\mathbf{Y} = \mathbf{y}$ , using the same DM-trained prior  $p_{\mathbf{z}}$  as for proj-TDPS, and the true Poisson log-posterior  $\nabla_{\mathbf{z}} \log p_{\mathbf{Y}|\mathbf{Z}=\mathbf{z}}(\mathbf{y})$ . This approach, which is the analogue of (11), is referred to as ODPS.

Section III-A introduces the basics on DMs and DPS in the context of im-TDPS, and ODPS. We do not describe proj-TDPS

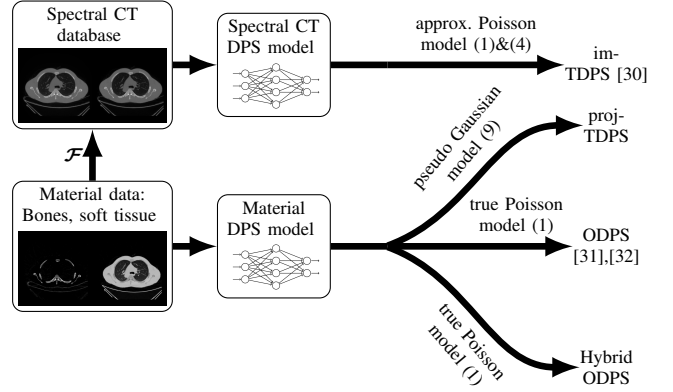


Fig. 2: Overview of the described DPS-based methods for MD. ODPS, Hybrid-ODPS and proj-TDPS share the same DM trained on material images. They differ by the model used to solve MD. The im-TDPS method uses a DM trained on spectral images for the two-step MD.

as it is similarly implemented as ODPS by replacing the log-prior  $\nabla_{\mathbf{z}} \log p_{\mathbf{Y}|\mathbf{Z}=\mathbf{z}}(\mathbf{y})$  with  $\nabla_{\mathbf{z}} \log p_{\mathbf{L}|\mathbf{Z}=\mathbf{z}}(\hat{\ell})$ . Section III-B introduces a heuristic method derived from ODPS to include additional materials that are not present in the training dataset. A variational regularizer is introduced for the added materials, while we keep the DM prior for the other material images. We refer to this method as Hybrid-ODPS.

Figure 2 presents an overview of the proposed methods.

### A. Standard Approach with all Materials Present in the Training Dataset

We denote by  $\mathbf{W} \in \{\mathbf{X}, \mathbf{Z}\}$  the random vector to be estimated by DPS, i.e. the pseudo-spectral images  $\mathbf{X}$  for im-TDPS (cf. (5)) and the material images  $\mathbf{Z}$  for ODPS (cf. (11)).

1) *Diffusion models (DMs)*: The training of a DM (cf. Ho *et al.* [19]) involves a diffusion process that incrementally adds noise to an initial image  $\mathbf{W}_0$ , sampled from the training dataset with PDF  $p^{\text{data}}$ ,

$$\mathbf{W}_t = \sqrt{\bar{\alpha}_t} \mathbf{W}_0 + \sqrt{1 - \bar{\alpha}_t} \boldsymbol{\epsilon}, \quad \boldsymbol{\epsilon} \sim \mathcal{N}(\mathbf{0}, \mathbf{I}) \quad (12)$$

where  $\bar{\alpha}_t = \prod_{s=1}^t \alpha_s$ ,  $\alpha_t \in [0, 1]$  being a monotonically decreasing sequence defined such that  $\bar{\alpha}_T = 0$  and  $T$  is the final step of the forward diffusion. An approximate reverse process, involving the score function  $\nabla \log p_{\mathbf{W}_t}$ , can be derived to sample  $\mathbf{W}_{t-1}$  from  $\mathbf{W}_t$  as

$$\mathbf{W}_{t-1} = \frac{\sqrt{\alpha_t}(1 - \bar{\alpha}_{t-1})}{1 - \bar{\alpha}_t} \mathbf{W}_t + \frac{\sqrt{\bar{\alpha}_{t-1}}(1 - \alpha_t)}{1 - \bar{\alpha}_t} \hat{\mathbf{w}}_0(\mathbf{W}_t) + \sigma_t \boldsymbol{\epsilon}_t, \quad \boldsymbol{\epsilon}_t \sim \mathcal{N}(\mathbf{0}, \mathbf{I}), \quad (13)$$

where  $\sigma_t = (1 - \alpha_t)(1 - \bar{\alpha}_{t-1})/(1 - \bar{\alpha}_t)$  and  $\hat{\mathbf{w}}_0(\mathbf{w}_t)$  is given by Tweedie's formula, i.e.,

$$\begin{aligned} \hat{\mathbf{w}}_0(\mathbf{w}_t, t) &:= \mathbb{E}[\mathbf{W}_0 | \mathbf{W}_t = \mathbf{w}_t] \\ &= \frac{\mathbf{w}_t + (1 - \bar{\alpha}_t) \nabla \log p_{\mathbf{W}_t}(\mathbf{w}_t)}{\sqrt{\bar{\alpha}_t}}. \end{aligned} \quad (14)$$

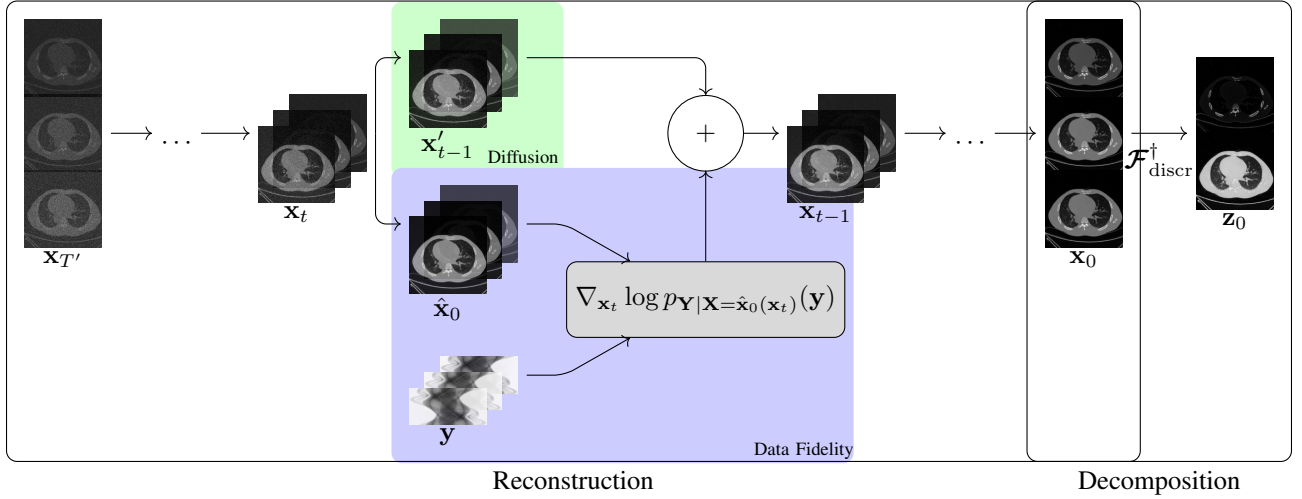


Fig. 3: Summary of the two-step im-TDPS method. The first step is the reconstruction of spectral images using the image domain formulation (5) with a prior learned by a diffusion model. Afterward, the material decomposition (6) is obtained with the pseudo inverse  $\mathcal{F}_{discr}^\dagger$ . In order to show the overall effect of the algorithm, images presented in this figure are 200 steps apart.

The score function  $\nabla \log p_{\mathbf{w}_t}$  is unknown and therefore is approximated by a convolutional neural network (CNN)  $\mathcal{S}_\theta(\cdot, t)$  trained by score matching as

$$\min_{\theta} \mathbb{E}_{t, \mathbf{w}_0, \mathbf{w}_t | \mathbf{w}_0} \left[ \left\| \mathcal{S}_\theta(\mathbf{w}_t, t) - \nabla \log p_{\mathbf{w}_t | \mathbf{w}_0}(\mathbf{w}_t) \right\|_2^2 \right] \quad (15)$$

where  $\mathbf{w}_0 \sim p^{\text{data}}$ ,  $p_{\mathbf{w}_t | \mathbf{w}_0}$  is given by (12) and  $t$  is uniformly sampled on  $[0, T]$ .

2) *Diffusion Posterior Sampling (DPS)*: It is possible to leverage the generative capability of a DM to regularize an inverse problem; see, for instance, [25], [26]. The idea is to condition the expectation (14) on the measurements  $\mathbf{Y} = \mathbf{y}$ . This leads to the conditional score  $p_{\mathbf{w}_t | \mathbf{Y}=\mathbf{y}}(\cdot)$ , which, thanks to Bayes' rule, can be written as

$$\begin{aligned} \nabla \log p_{\mathbf{w}_t | \mathbf{Y}=\mathbf{y}}(\mathbf{w}_t) &= \nabla \log p_{\mathbf{w}_t}(\mathbf{w}_t) \\ &\quad + \nabla_{\mathbf{w}_t} \log p_{\mathbf{Y} | \mathbf{w}_t}(\mathbf{y}) \end{aligned}$$

where the subscript  $\mathbf{w}_t$  was added on  $\nabla$  to specify the variable of differentiation. The first term  $\nabla(\log p_{\mathbf{w}_t})(\mathbf{w}_t)$  is the unconditional score which is approximated by  $\mathcal{S}_\theta(\mathbf{w}_t, t)$ . The second term  $\nabla_{\mathbf{w}_t}(\log p_{\mathbf{Y} | \mathbf{w}_t}(\mathbf{y}))$  is untractable.

In this work, we used the DPS approximation [28], i.e.,

$$\nabla_{\mathbf{w}_t} \log p_{\mathbf{Y} | \mathbf{w}_t}(\mathbf{y}) \approx \nabla_{\mathbf{w}_t} (\log p_{\mathbf{Y} | \mathbf{w}=\hat{\mathbf{w}}_0(\mathbf{w}_t)}(\mathbf{y})) \quad (16)$$

which is derived from the gradient of the log-likelihood  $\log p_{\mathbf{Y} | \mathbf{W}}$  given by forward model (1) (for  $\mathbf{W} = \mathbf{Z}$ ) or (4) (for  $\mathbf{W} = \mathbf{X}$ ). The approximate conditional score is then added to the reverse process (13) in order to generate a sample from  $p_{\mathbf{W} | \mathbf{Y}=\mathbf{y}}$ . Therefore, DPS alternates between sampling (13) and performing a gradient ascent step using (16).

Using the DPS method, we implemented (i) im-TDPS to sample  $\mathbf{W} = \mathbf{X}$  from  $p_{\mathbf{X} | \mathbf{Y}=\mathbf{y}}$ , followed by the application of the pseudo-inverse  $\mathcal{F}_{discr}^\dagger$  in order to obtain material images  $\mathbf{z}$  (cf. Figure 3), and (ii) ODPS to directly sample  $\mathbf{W} = \mathbf{Z}$  from

$p_{\mathbf{Z} | \mathbf{Y}=\mathbf{y}}$  (cf. Figure 4). The implementation of proj-TDPS is similar to that of ODPS and is shown on the same figure.

### B. Hybridization with Variational Regularizer for Untrained Additional Materials

DPS methods are limited to MD using models trained on databases that contain images of the same materials. However, there are scenarios where MD may need to include additional materials not present in the training dataset. For example, a model trained on images of bone and soft tissue may be required to be applied to a patient administered with an iodine tracer. In this section we present a heuristic technique for ODPS and im-TDPS, namely Hybrid-ODPS, to address this case which somehow resembles to DPS for solving blind inverse problems [38], [39].

We consider the random material image  $[\mathbf{Z}, \tilde{\mathbf{Z}}]$ , where  $\mathbf{Z}$  represents the  $n_m$  materials present in the training database, and  $\tilde{\mathbf{Z}}$  represents the  $\tilde{n}_m$  materials unknown to the model. The trained model can be used to sample  $\mathbf{Z} \sim p_{\mathbf{Z}}$ . In order to sample  $(\mathbf{Z}, \tilde{\mathbf{Z}}) \sim p_{\mathbf{Z}, \tilde{\mathbf{Z}}}$ , the conditional PDF  $p_{\tilde{\mathbf{Z}} | \mathbf{Z}}$  is needed, but unknown. We therefore assume that  $\mathbf{Z}$  and  $\tilde{\mathbf{Z}}$  are independent, i.e.

$$p_{\mathbf{Z}, \tilde{\mathbf{Z}}}(\mathbf{z}, \tilde{\mathbf{z}}) = p_{\mathbf{Z}}(\mathbf{z}) \cdot p_{\tilde{\mathbf{Z}}}(\tilde{\mathbf{z}}).$$

This hypothesis is obviously incorrect (for example, iodine is only present in soft tissues, which is a form of dependence). However, we will see later that this hypothesis leads to a reasonable algorithm. Another issue is that  $p_{\tilde{\mathbf{Z}}}(\tilde{\mathbf{z}})$  is also unknown. We therefore replace it with a pseudo PDF  $\tilde{p}$  of the form

$$\tilde{p}(\tilde{\mathbf{z}}) \propto e^{-R(\tilde{\mathbf{z}})}$$

where  $R: \mathbb{R}^{n_p \times \tilde{n}_m} \rightarrow \mathbb{R}$  is a convex edge-preserving regularizer such as for example the Huber penalty [40], [41]. Note that  $\tilde{p}$  is not a PDF as it may integrate to infinity. As  $\mathbf{Z}$  and  $\tilde{\mathbf{Z}}$

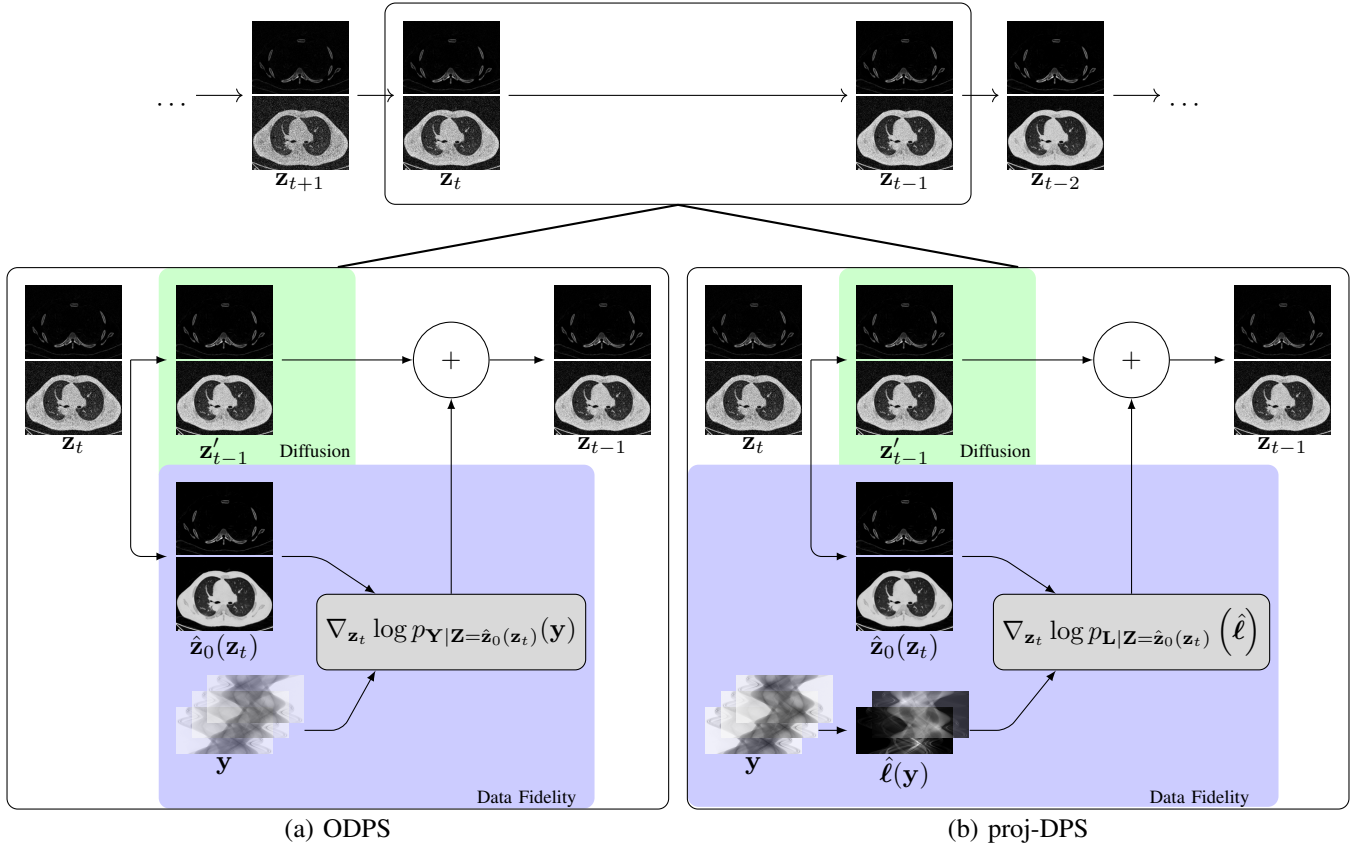


Fig. 4: Summary of the ODPS and proj-TDPS methods. First row is the global reverse diffusion process. Second row presents one iteration of (a) ODPS and (b) proj-TDPS. For proj-TDPS, the data fidelity term is applied on an approximation  $\hat{\ell}(\mathbf{y})$  of the material sinograms obtained by solving (7). In order to show the overall effect of both algorithms, images presented in this Figure are 200 steps apart.

are independent, the estimates  $\mathbf{Z}_t$  and  $\tilde{\mathbf{Z}}_t$  at time  $t$  of the DM are also independent. The conditional score at time  $t$  can be written as

$$\begin{aligned} & \nabla_{\mathbf{z}_t, \tilde{\mathbf{z}}_t} \log p_{\mathbf{Z}_t, \tilde{\mathbf{Z}}_t | \mathbf{Y}=\mathbf{y}}(\mathbf{z}_t, \tilde{\mathbf{z}}_t) \\ &= \begin{bmatrix} \nabla \log p_{\mathbf{Z}_t}(\mathbf{z}_t) + \nabla_{\mathbf{z}_t} \log p_{\mathbf{Y} | (\mathbf{Z}_t, \tilde{\mathbf{Z}}_t)=(\mathbf{z}_t, \tilde{\mathbf{z}}_t)}(\mathbf{y}) \\ \nabla \log p_{\tilde{\mathbf{Z}}_t}(\tilde{\mathbf{z}}_t) + \nabla_{\tilde{\mathbf{z}}_t} \log p_{\mathbf{Y} | (\mathbf{Z}_t, \tilde{\mathbf{Z}}_t)=(\mathbf{z}_t, \tilde{\mathbf{z}}_t)}(\mathbf{y}) \end{bmatrix}. \end{aligned}$$

The score function  $\nabla \log p_{\mathbf{Z}_t}(\mathbf{z}_t)$  corresponding to the  $n_m$  materials present in the training dataset is approximated by  $\mathcal{S}_\theta(\mathbf{z}_t, t)$  trained as (15) while the conditional score functions  $\nabla_{\mathbf{z}_t} \log p_{\mathbf{Y} | (\mathbf{Z}_t, \tilde{\mathbf{Z}}_t)=(\mathbf{z}_t, \tilde{\mathbf{z}}_t)}$  and  $\nabla_{\tilde{\mathbf{z}}_t} \log p_{\mathbf{Y} | (\mathbf{Z}_t, \tilde{\mathbf{Z}}_t)=(\mathbf{z}_t, \tilde{\mathbf{z}}_t)}$  can be approximated using the forward model (i.e., in a similar fashion as in (16)). The score function  $\nabla \log p_{\tilde{\mathbf{Z}}_t}(\tilde{\mathbf{z}}_t)$  is unknown but can be approximated by  $\nabla \log p_{\tilde{\mathbf{Z}}}(\tilde{\mathbf{z}}_t) = -\nabla R(\tilde{\mathbf{z}}_t)$ . This leads to the following update rule for  $\tilde{\mathbf{z}}$  (with an added gradient step  $\xi_t$  on the log-prior  $R$ ):

$$\tilde{\mathbf{z}}_{t-1} = \tilde{\mathbf{z}}_t + \nabla_{\tilde{\mathbf{z}}_t} \log p_{\mathbf{Y} | (\mathbf{Z}, \tilde{\mathbf{Z}})=(\mathbf{z}_t, \tilde{\mathbf{z}}_t)} - \xi_t \nabla R(\tilde{\mathbf{z}}_t). \quad (17)$$

In summary, this approach is equivalent to performing an iterative algorithm to optimize a fitness function consisting of a data fidelity term and a regularizer in parallel to performing DPS. It should be noted that the gradient step (17) can be replaced with any optimization algorithm on the penalized

log-likelihood, and in this work we used an L-BFGS algorithm initialized from  $\tilde{\mathbf{z}}_t$ .

### C. Summary of the Algorithm

The overall algorithm for ODPS is summarized in Algorithm 1. Im-TDPS is implemented in a similar fashion but with  $\mathbf{x}_t$  instead of  $\mathbf{z}_t$ , followed by an image-based MD. The initial material image  $\tilde{\mathbf{z}}^{\text{init}}$  (corresponding to the materials absent from the training dataset) can be obtained with any standard MD technique. In this work we use an image-based MD on energy-discretized images  $\hat{\mathbf{x}}_k$  reconstructed from  $\mathbf{y}_{:,k}$  by filtered backprojection (FBP). The proj-TDPS method uses DPS prior learned on spectral images  $\mathbf{X}$  for solving (6), then, the pseudo inverse  $\mathcal{F}_{\text{discr}}^\dagger$  of the composition matrix is applied to obtain material images. Furthermore, we use the “jump start strategy” from Jiang *et al.* [42], starting from  $T' < T$  with a scout MD (from the FBP method) diffused to time  $T'$  using (12) (not shown in Algorithm 1). Finally, the log-likelihood gradient (16) is further approximated with differentiation with respect to  $\tilde{\mathbf{z}}_0$  instead of  $\mathbf{z}_t$  following the strategy of Jiang *et al.* [42]; this prevents differentiation through the NN.

---

**Algorithm 1** ODPS
 

---

**Require:**  $T, \theta, \mathbf{y}, \{\xi_t\}_{t=1}^T, \{\zeta_t\}_{t=1}^T, \{\sigma_t\}_{t=1}^T, \{\alpha_t\}_{t=1}^T, \bar{\mathbf{z}}^{\text{init}}$

- 1:  $\mathbf{z}_T \leftarrow \mathbf{Z}_t \sim \mathcal{N}(\mathbf{0}, \mathbf{I})$
- 2: **if**  $\bar{n}_m > 0$  **then**
- 3:    $\bar{\mathbf{z}}_T \leftarrow \bar{\mathbf{z}}^{\text{init}}$
- 4: **end if**
- 5: **for**  $t = T$  **to** 1 **do**
- 6:    $\hat{\mathbf{z}}_0 \leftarrow \frac{1}{\sqrt{\alpha_t}} (\mathbf{z}_t + (1 - \bar{\alpha}_t) \mathcal{S}_\theta(\mathbf{z}_t, t))$
- 7:    $\epsilon \sim \mathcal{N}(\mathbf{0}, \mathbf{I})$
- 8:    $\mathbf{z}'_t \leftarrow \frac{\sqrt{\alpha_t}(1 - \bar{\alpha}_{t-1})}{1 - \bar{\alpha}_t} \mathbf{z}_t + \frac{\sqrt{\bar{\alpha}_{t-1}}(1 - \alpha_t)}{1 - \bar{\alpha}_t} \hat{\mathbf{z}}_0 + \sigma_t \epsilon$
- 9:   **if**  $\bar{n}_m > 0$  **then**
- 10:      $\mathbf{z}_{t-1} \leftarrow \mathbf{z}'_t + \zeta_t \nabla_{\mathbf{z}_t} \log p_{\mathbf{Y}|\mathbf{Z}}(\mathbf{Z}, \bar{\mathbf{z}}) = (\hat{\mathbf{z}}(\mathbf{z}_t), \bar{\mathbf{z}}_t)(\mathbf{y})$
- 11:      $\bar{\mathbf{z}}_{t-1} \leftarrow \bar{\mathbf{z}}_t + \nabla_{\bar{\mathbf{z}}_t} \log p_{\mathbf{Y}|\mathbf{Z}}(\mathbf{Z}, \bar{\mathbf{z}}) = (\mathbf{z}_t, \bar{\mathbf{z}}_t) - \xi_t \nabla R(\bar{\mathbf{z}}_t)$
- 12:   **else**
- 13:      $\mathbf{z}_{t-1} \leftarrow \mathbf{z}'_t + \zeta_t \nabla_{\mathbf{z}_t} \log p_{\mathbf{Y}|\mathbf{Z}}(\mathbf{z} = \hat{\mathbf{z}}(\mathbf{z}_t))(\mathbf{y})$
- 14:   **end if**
- 15: **end for**

---

## IV. RESULTS

All reconstruction methods and simulations were implemented in Python. The models were implemented and trained using Pytorch, and we used TorchRadon [43] for the two-dimensional (2-D) CT fan-beam projector  $\mathcal{A}$ .

Our projector incorporates 750 detectors, each with a width of 1.2 mm, with source-to-origin of 624 mm and origin-to-detector of 325 mm [44].

We used the structural similarity index measure (SSIM) and the peak signal-to-noise ratio (PSNR) from the `skimage.metrics` library as metrics for evaluation. In addition, we used learned perceptual image patch similarity (LPIPS) from Zhang *et al.* [45] with the version 0.1 of AlexNet NN, where each image was linearly scaled to  $[-1, 1]$ . The metrics were computed with respect to a material reference image obtained during the data preparation.

### A. Data Preparation

We considered  $n_m = 2$  materials: soft tissues and bones. The mass attenuation coefficients of the materials used to define  $\mathcal{F}$  with a 1-keV energy discretization were derived using the Spektr toolkit [46].

The dataset used for this experiment consists of 11 three-dimensional (3-D) chest CT patient images for five full-dose energy bins (40, 60, 80, 100 and 120 keV) acquired on a Philips IQon Spectral CT from Poitiers University Hospital, France. We performed three partitions of the dataset where, for each partition, one patient is kept for testing while the other patients are used for training all NN models. Therefore, for each partition, models were trained on 9 patients and tested on one patient. Each 3-D volume comprises approximately 350 slices of dimension 512×512 with 1-mm pixel size, thus leading to a testing dataset comprising approximately 1,000 images. The results presented in Tables II, III and IV as well as in Figures 6, 8 and 10 were averaged over all the slices of all the testing patients.

Material images for training and for reference were obtained by applying  $\mathcal{F}_{\text{discr}}^\dagger$  onto the clean attenuation images. The PCCT simulated  $\mathbf{y}_k$  measurements are generated from the reference material images  $\mathbf{z}$  using the forward model described in (1) and (2).

For Experiment 1 (Section IV-C) the data were generated from bones and soft tissues using the energy spectrum shown in Figure 1 with  $n_e = 3$  energy bins: 10–40 keV, 40–60 keV and 60–120 keV. We considered two cases: (i) full-view (360 angles) and (ii) sparse-view (60 angles). The total expected number of photons is  $\sum_k \int h_k(e) de \approx 55,000$  for both (i) and (ii) in order to simulate a low-dose setting.

For Experiment 2 (Section IV-D) we considered additional artificial iodine distributions, with the same the energy spectrum as in Experiment 1 but with  $n_e = 6$  energy bins obtained by splitting the energy bins of the previous experiment in two interval of the same length. The artificial iodine distributions were created as a random number (between 2 and 5) of randomly generated shapes within the soft tissue, with peak value at the center of each shape and decreasing towards the edge. Hybrid-ODPS was implemented with the Huber regularizer for iodine (cf.  $R$  in (III-B)).

### B. Reconstruction Methods for Comparison

We compared three DPS methods (ODPS, im-TDPS and proj-TDPS) with other two-step decomposition methods as well as a one-step variational method, described in the following subsections. Each method is finely-tuned with respect to the above-mentioned metrics. Both ODPS and proj-TDPS use a NN trained on material images, while im-TDPS uses a NN trained on spectral images. Hybrid-ODPS was compared with L-BFGS (see Section IV-B1 for description).

1) *One-step approaches:* We used the quasi-Newton L-BFGS [36] to solve (11) where the regularizer (i.e., the negative log-prior) is defined with a mix of Huber regularization [41] on image gradients and inner product regularization between pair of material images to promote material separability and mitigate crosstalks [47].

L-BFGS was used in Experiment 1 and 2.

2) *Two-step approaches:* We present here the two-step methods, which are also listed in Table I. These methods were used in Experiment 1 only.

a) *FBP:* The FBP approach consists in performing the analytical inversion of the projector  $\mathcal{A}$ , denoted  $\mathcal{A}^\dagger$ , applied to the approximated sinograms  $\mathbf{b}_k = [b_{1,k}, \dots, b_{n_b,k}] \in \mathbb{R}^{n_b}$ , where  $b_{i,k} = \log \bar{h}_k / y_{i,k}$  for all  $(i, k)$ , derived from the measurements  $\mathbf{y} = \{\mathbf{y}_k\}_{k=1}^{n_e}$ . It is then followed by the application of  $\mathcal{F}_{\text{discr}}^\dagger$  to decompose the (pseudo-)spectral images into material images:

$$\hat{\mathbf{x}} = \left\{ \mathcal{A}^\dagger(\mathbf{b}_k) \right\}_{k=1, \dots, n_e},$$

$$\hat{\mathbf{z}} = \mathcal{F}_{\text{discr}}^\dagger(\hat{\mathbf{x}}).$$

b) *U-Net-I and U-Net-P:* Inspired from Abascal *et al.* [16], we implemented two additional AI-based methods that use the U-Net architecture. U-Net-I is a CNN that preforms material decomposition in the image domain (i.e., from the multi-energy images  $\mathbf{x}_k, k = 1, \dots, n_e$ ) while U-Net-P is a CNN decomposes the material in the projection domain to provide the material sinograms for reconstruction. We used L-BFGS with a Huber regularizer as negative log-prior for the ‘reconstruction’ steps of U-Net-I (i.e, solving (5)) and U-Net-P (i.e., solving (10)).

Method	Step 1		Step 2	
	Recon.	Reg.	Recon.	Reg.
FBP	FBP	$\emptyset$	$\mathcal{F}^{\text{discr}}$	$\emptyset$
Im-TDPS	DPS	DM	$\mathcal{F}^{\text{discr}}$	$\emptyset$
U-Net-I	L-BFGS	Huber	U-Net-I	NN
	Decomp.		Recon.	
Proj-TDPS	L-BFGS	Huber	DPS	DM
U-Net-P	U-Net-P	NN	FBP	$\emptyset$

TABLE I: Experiment 1—List of the two-step material decomposition methods we used for comparison.

### C. Experiment 1—Results with no added materials ( $\tilde{n}_m = 0$ )

1) *Full-view Data*: Figure 5 shows the images of the reconstructed material on one slice of the test dataset with the proposed methods. The FBP-reconstructed images suffer from noise amplification. This results from the direct inversion of  $\mathcal{A}$  which then propagates in the material images. Noise amplification is somehow mitigated in the L-BFGS reconstruction thanks to the regularizer and the use of the true forward model with true statistics.

U-Net-I and U-Net-P produce sharp images that appear fairly similar to the reference images. The im-TDPS-reconstructed images suffer from crosstalk (i.e., bones visible in the soft tissue image) which can be attributed to the simplified forward model (4) (in which the X-ray emission is assumed to be monochromatic for each bin) while proj-TDPS produces accurate images. Note that proj-TDPS uses the same diffusion prior as ODPS but the data-fidelity term is derived from the approximate model (9) that does not utilize the true statistics of the measurement, which could explain the slight decrease in image quality. On the other end, ODPS uses the true forward model and therefore produces sharp and noise-free images. Table II presents the PSNR, SSIM and LPIPS metrics averaged on the test dataset for each of the methods presented as well as the average computational time. The metrics were computed for each material separately. They corroborate the observations from Figure 5 with ODPS outperforming all other methods, with the exception of PSNR and SSIM for soft tissue where ODPS is slightly outperformed by U-Net-I.

Figure 6 presents boxplots computed over the training dataset for all metrics and material (we omitted FBP as it is largely outperformed). Surprisingly, AI-based methods have a low variability compared to L-BFGS. We believe that this could be explained by the noisy FBP initialization of L-BFGS which increases its randomness.

2) *Sparse-view Data*: Figure 7 and Table III present the result for the sparse-view experiment.

FBP images suffer from noise and streak artifacts. The L-BFGS MD manages to keep the noise under control but the material images suffer from streak artifacts as the handcrafted regularizer is primarily designed to process Gaussian noise; this can be addressed with MD combining the data-fidelity term with total variation (TV) regularizers, which can be optimized with a primal-dual algorithm [48] or the alternating direction method of multipliers [49].

U-Net-I produces oversmoothed images compared to the previous experiment. This is because we increased the strength of the regularizer to compensate for the sparsity of the mea-

surement, which produces streak artifacts in the reconstruction step. For U-Net-P, we reduced the strength of the regularizer to improve the metrics, resulting in artifacts in the images. In both case, a TV regularizer in the reconstruction step can potentially mitigate these effects.

While im-TDPS suffers from the same crosstalks as in the full-view case and proj-TDPS has from some minor artifacts (cf. green magnified area), the ODPS reconstruction is accurate.

Table III shows the same metrics as Table II for the sparse-view data. The results are similar; except that this time ODPS outperforms all methods.

Figure 8 presents the boxplots of the metric obtained, and are similar to those of Figure 6.

### D. Experiment 2—Hybridization with added Iodine

We used the same imaging setup as in the full-view experiment with two materials.

We set the parameters and weight of the Huber regularizer on the iodine channel to be the same between both Hybrid-ODPS and L-BFGS so that the main difference between the two is the prior on the bones and soft tissue channels. For this experiment the metrics were computed on a region that excludes the bed.

Figure 9 shows the results on one slice. Rows 1 and 2 show bones and soft tissue material maps, which were used to train the DPS model, while Row 3 shows the iodine map which was only present to create the measurement  $\mathbf{y}$  used for inference.

Compared to L-BFGS, Hybrid-ODPS shows reduced noise, particularly on the soft tissue and iodine distributions. Hybrid-ODPS outperforms L-BFGS on soft tissues and iodine with all metrics, and shows similar results on the bone distribution. Table IV and Figure 10 confirm these observations.

When comparing line profiles, Hybrid-ODPS is similar to the reference image, while L-BFGS shows noise amplification in the soft tissue and iodine images. Both Hybrid-ODPS and L-BFGS have similar lower absolute values for all material images.

Some crosstalk in the iodine image is observed in both the Hybrid-ODPS method and L-BFGS. This occurs due to the similar energy-dependent mass attenuation of the two materials and the absence of a trained prior on iodine distribution in the Hybrid ODPS method. As a result, bone density is generally underestimated in regions where this crosstalk appears, as shown in the profile in Figure 9.

It should be remarked that in general, the metrics results show lower values for PSNR and SSIM, and higher values for LPIPS compared to experiment 1, as the addition of the third material makes the problem more complex.

This experiment shows that Hybrid-ODPS is a viable alternative to L-BFGS as it retains advantages of ODPS while incorporating a material that was not present during model training.

## V. DISCUSSION

The one-step methods generally give better results than two-step methods as already mentioned in previous articles on this subject [14], [37]. We believe that combining a strong prior

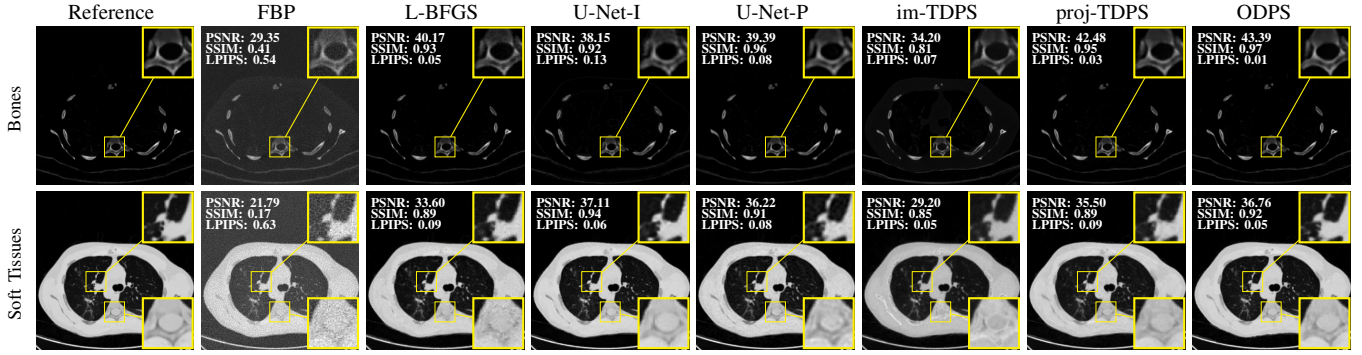


Fig. 5: Experiment 1 (full-view data)—Material decomposition images obtained with the different methods.

		FBP	L-BFGS	U-Net-I	U-Net-P	im-TDPS	proj-TDPS	ODPS
Avg. Time (in sec)		0.06	28.59	95.91	88.26	90.51	89.3	134.08
PSNR $\uparrow$	Bones	26.41	37.97	39.99	<b>42.48</b>	30.12	41.39	<u>42.13</u>
	Tissues	20.74	31.31	33.06	33.05	25.78	<u>34.52</u>	<b>35.86</b>
SSIM $\uparrow$	Bones	0.26	0.89	0.90	<b>0.96</b>	0.64	0.91	<u>0.95</u>
	Tissues	0.12	0.80	<u>0.86</u>	0.79	0.56	<b>0.87</b>	<b>0.87</b>
LPIPS $\downarrow$	Bones	0.64	0.10	0.07	0.06	0.09	<u>0.04</u>	<b>0.02</b>
	Tissues	0.68	0.17	0.12	0.21	0.10	<b>0.04</b>	<u>0.06</u>

TABLE II: Experiment 1 (full-view data)—Averaged performance metrics computed over the entire test dataset. Best and second best results are respectively in bold and underlined.

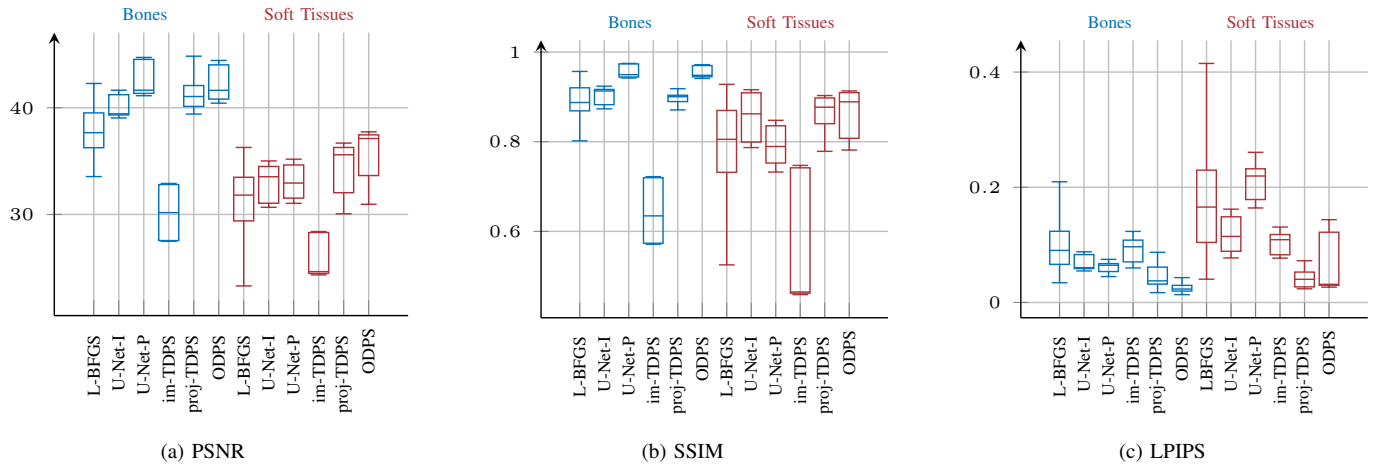


Fig. 6: Experiment 1 (full-view data)—Boxplots of (a) PSNR, (b) SSIM and (c) LPIPS, computed over the test dataset.

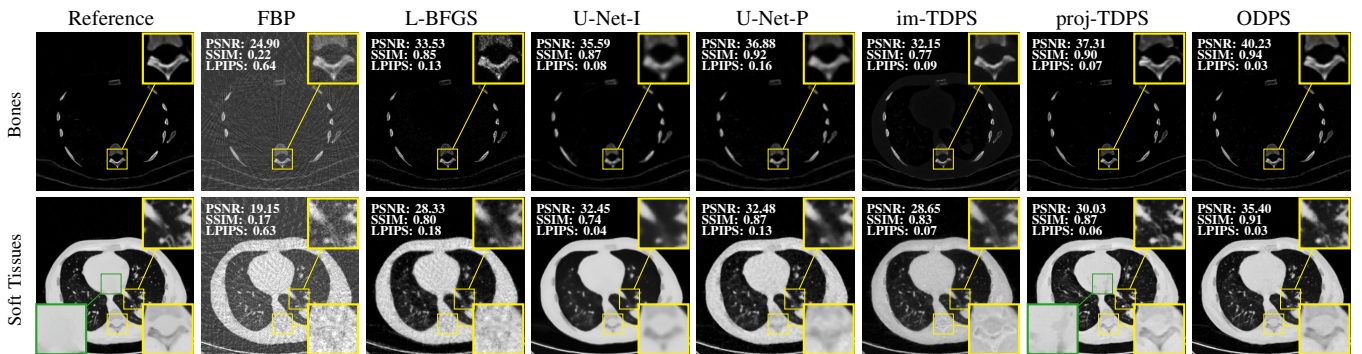


Fig. 7: Experiment 1 (sparse-view data)—Material decomposition images obtained with the different methods.

		FBP	L-BFGS	U-Net-I	U-Net-P	im-TDPS	proj-TDPS	ODPS
Avg. Time (in sec)		0.05	23.67	104.38	105.35	90.38	82.97	88.89
PSNR $\uparrow$	Bones	25.22	35.09	37.52	<b>41.29</b>	30.09	37.69	<u>40.58</u>
	Tissues	19.13	29.57	33.35	32.46	25.55	31.48	<b>35.05</b>
SSIM $\uparrow$	Bones	0.22	0.87	<u>0.93</u>	<b>0.94</b>	0.64	0.90	<b>0.94</b>
	Tissues	0.11	0.78	<b>0.90</b>	0.83	0.55	0.82	<u>0.86</u>
LPIPS $\downarrow$	Bones	0.69	0.11	0.08	0.08	0.09	<u>0.07</u>	<b>0.04</b>
	Tissues	0.67	0.18	0.08	0.16	0.11	<b>0.06</b>	<u>0.07</u>

TABLE III: Experiment 1 (sparse-view data)—Averaged performance metrics computed over the entire test dataset. Best and second best results are respectively in bold and underlined.

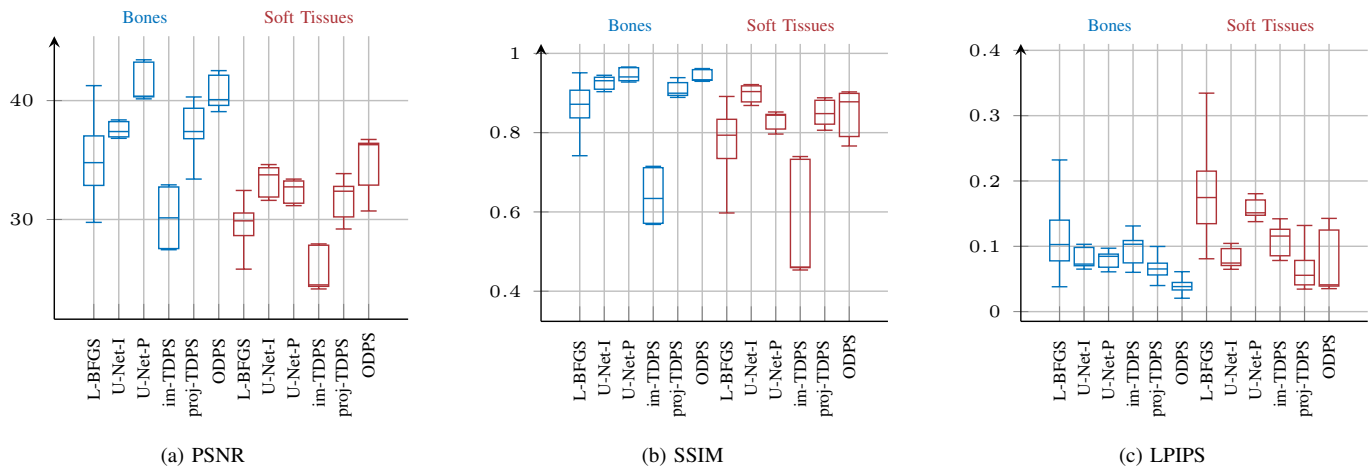


Fig. 8: Experiment 1 (sparse-view data)—Boxplots of (a) PSNR, (b) SSIM and (c) LPIPS, computed over the test dataset.

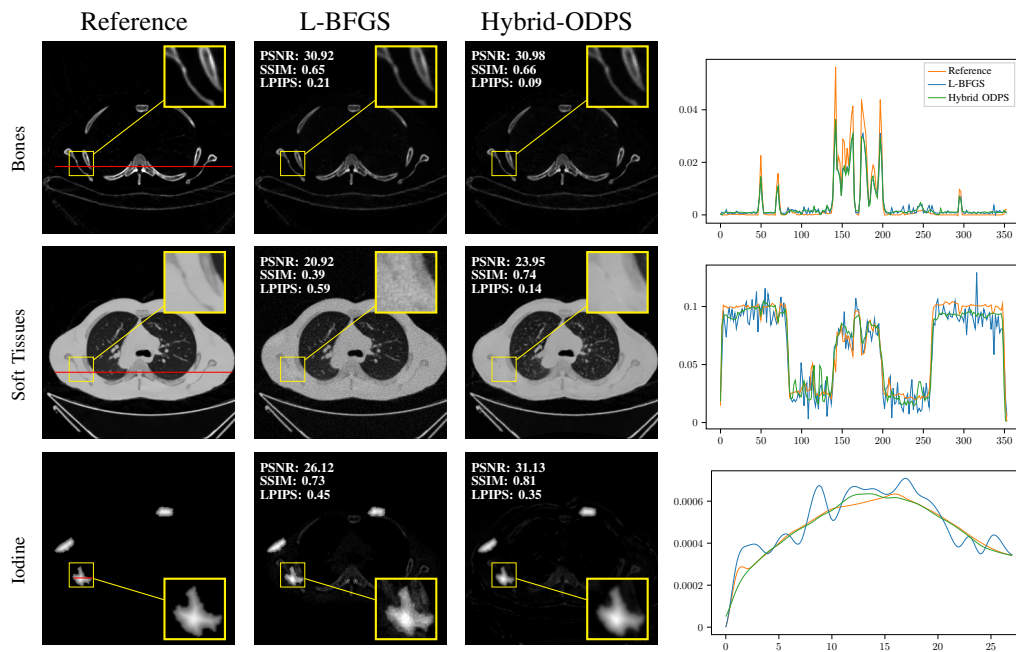


Fig. 9: Experiment 2—Hybrid-ODPS and L-BFGS material images as well as their associated metrics and density profiles. The red line on the reference image indicates the location of the density profile.

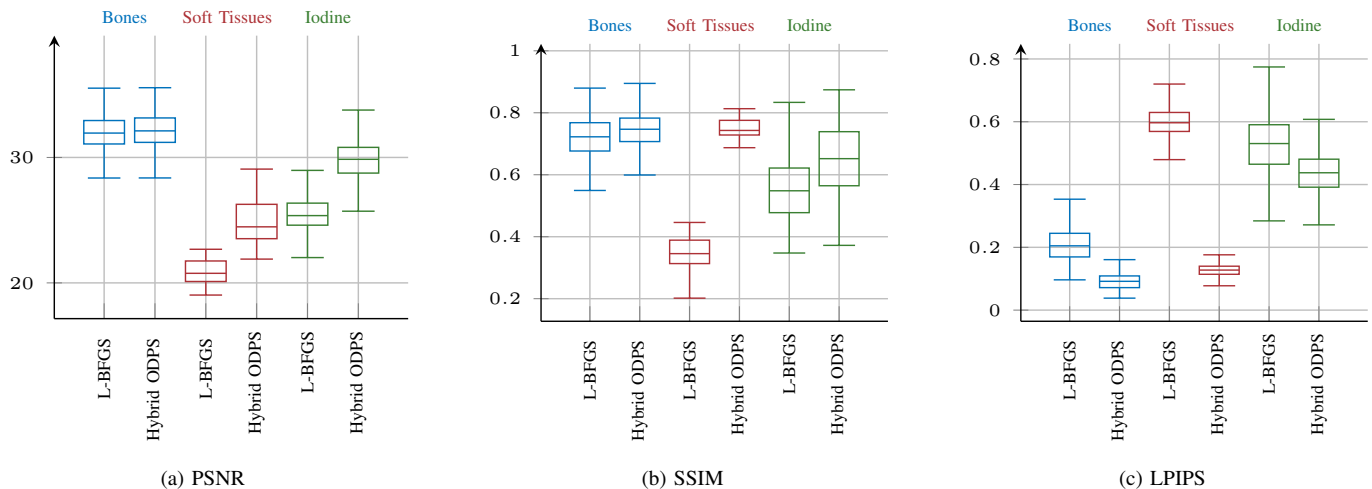


Fig. 10: Experiment 2—Boxplots of (a) PSNR, (b) SSIM and (c) LPIPS computed over the test dataset.

		L-BFGS	Hybrid ODPS
PSNR $\uparrow$	Bones	32.00	<b>32.16</b>
	Tissues	21.53	<b>25.39</b>
	Iodine	25.54	<b>29.79</b>
SSIM $\uparrow$	Bones	0.72	<b>0.74</b>
	Tissues	0.37	<b>0.76</b>
	Iodine	0.56	<b>0.65</b>
LPIPS $\downarrow$	Bones	0.21	<b>0.09</b>
	Tissues	0.60	<b>0.13</b>
	Iodine	0.53	<b>0.44</b>

TABLE IV: Experiment 2 (Hybridization with iodine)—Averaged metrics computed over the test dataset.

learned using DM with the one-step forward model (11) is crucial in order to obtain satisfactory results. As we showed, relying only on DM is not sufficient as im-TDPS and proj-TDPS suffer from either crosstalk for the former and slight over-smoothing for the latter. These results contrast with our previous work [32] where the performance of im-TDPS was comparable with ODPS; this is because we used a monochromatic model for each energy bin in [32] while in this work we used a realistic polychromatic model.

In addition, we showed that priors learned on material images are more important and impactful than priors learned on spectral images. Indeed, proj-TDPS (resp. U-Net-I) delivers better results than im-TDPS (resp. U-Net-P). As noted in [16], it is easier to learn a material image prior than a material projection prior (as U-Net-P does). Furthermore, in the case of two-step methods, a learned prior for MD is better than a learned prior for image reconstruction as U-Net methods produce better results than im-TDPS. Finally, we worked on 2-D slices instead of the full 3-D volume as DM are computationally expensive. Even on 2-D slices, DPS methods are time consuming. Table II (full-view setting) suggests that ODPS requires a larger computational time than other methods. However, this gap decreases in Table III (sparse-view setting). We believe that a smaller sinogram size decreases the computational time of the log-likelihood gradient. The im-TDPS method is not impacted by this change as it

operates on the image domain which is the same for both sparse and full-view settings. In addition, we performed all methods sequentially, one slice at the time. We believe that by leveraging parallelization, MD on multiple slices can be performed simultaneously, thus significantly decreasing the computational time at the expense of higher memory cost. Methods such as wavelets DMs [50]–[53], cascaded DMs [54] or diffusion Schrödinger bridge [55], denoising diffusion implicit models [56], could also be considered to accelerate the methods or even work directly on 3-D volumes.

To our knowledge, the proposed Hybrid-ODPS method is the first to combine a DM-based learned prior with conventional regularization for out-of-database channels during inference. Barbano *et al.* [57] propose to train a model on synthetic data and then to adapt it during the inference step to solve inverse problems in the case where there are few high-quality data available. As Hybrid-ODPS is agnostic to the choice of material we believe it can be applied to any scenario with materials other than contrast agent that are not present in training data.

For the case of contrast-enhanced spectral CT, we believe the large amount of data available for bones and soft tissues justifies the proposed Hybrid-ODPS. The choices made to regularize the iodine image need to be further evaluated. In particular, the Huber penalty used treats each material channel independently. Hybrid-ODPS also allows regularizations that takes into account joint information (e.g., inner-product regularization [47]). Finding the optimal regularizers and weights for each specific task remains a challenge, and this particular task requires further investigation.

## VI. CONCLUSION

This study explored multiple DPS-based approaches for MD in PCCT, evaluating their performance against traditional variational and AI-based techniques. The results demonstrate that ODPS provides the best overall performance, producing high-quality material maps with minimal noise and artifact contamination. Furthermore, the Hybrid-ODPS method successfully extends the applicability of DPS to materials absent

from the training set, providing a practical solution for real-world clinical and research scenarios.

The findings highlight the potential of diffusion models as powerful regularizers for inverse problems in medical imaging. Given the promising results, future research should focus on improving computational efficiency and exploring the integration of DPS with real-time imaging applications. Additionally, further validation on clinical datasets will be necessary to confirm the generalizability of these methods in diverse imaging conditions.

#### ACKNOWLEDGMENT

All authors declare that they have no known conflicts of interest in terms of competing financial interests or personal relationships that could have an influence or are relevant to the work reported in this article.

#### REFERENCES

- [1] K. Taguchi and J. S. Iwaczyk, "Vision 20/20: Single photon counting x-ray detectors in medical imaging," *Medical Physics*, vol. 40, no. 10, p. 100901, 2013. DOI: <https://doi.org/10.1118/1.4820371>. eprint: <https://aapm.onlinelibrary.wiley.com/doi/pdf/10.1118/1.4820371>. [Online]. Available: <https://aapm.onlinelibrary.wiley.com/doi/abs/10.1118/1.4820371>.
- [2] A. Bousse, V. S. S. Kandarpa, S. Rit, A. Perelli, M. Li, G. Wang, J. Zhou, and G. Wang, "Systematic review on learning-based spectral CT," *IEEE Transactions on Radiation and Plasma Medical Sciences*, 2023. DOI: 10.1109/TRPMS.2023.3314131. [Online]. Available: <https://arxiv.org/abs/2304.07588>.
- [3] D. S. Rigie and P. J. L. Rivière, "Joint reconstruction of multi-channel, spectral CT data via constrained total nuclear variation minimization," *Physics in Medicine & Biology*, vol. 60, no. 5, p. 1741, Feb. 2015. DOI: 10.1088/0031-9155/60/5/1741.
- [4] W. Wu, Y. Zhang, Q. Wang, F. Liu, P. Chen, and H. Yu, "Low-dose spectral CT reconstruction using image gradient l0-norm and tensor dictionary," *Applied Mathematical Modelling*, vol. 63, pp. 538–557, 2018, ISSN: 0307-904X. DOI: <https://doi.org/10.1016/j.apm.2018.07.006>. [Online]. Available: <https://www.sciencedirect.com/science/article/pii/S0307904X18303135>.
- [5] A. Perelli, S. A. Garcia, A. Bousse, J.-P. Tasu, N. Efthimiadis, and D. Visvikis, "Multi-channel convolutional analysis operator learning for dual-energy CT reconstruction," *Physics in Medicine & Biology*, vol. 67, no. 6, p. 065001, 2022.
- [6] R. E. Alvarez and A. Macovski, "Energy-selective reconstructions in X-ray computerized tomography," *Physics in Medicine & Biology*, vol. 21, no. 5, p. 733, Sep. 1976. DOI: 10.1088/0031-9155/21/5/002.
- [7] D. P. Cormode, E. Roessl, A. Thrän, T. Skajaa, R. E. Gordon, J.-P. Schlomka, V. Fuster, E. A. Fisher, W. J. Mulder, R. Proksa, *et al.*, "Atherosclerotic plaque composition: Analysis with multicolor CT and targeted gold nanoparticles," *Radiology*, vol. 256, no. 3, pp. 774–782, 2010.
- [8] A. N. Primak, J. G. Fletcher, T. J. Vrtiska, O. P. Dzyubak, J. C. Lieske, M. E. Jackson, J. C. Williams Jr, and C. H. McCollough, "Noninvasive differentiation of uric acid versus non-uric acid kidney stones using dual-energy CT," *Academic radiology*, vol. 14, no. 12, pp. 1441–1447, 2007.
- [9] A. Graser, T. R. Johnson, M. Bader, M. Staehler, N. Haseke, K. Nikolaou, M. F. Reiser, C. G. Stief, and C. R. Becker, "Dual energy CT characterization of urinary calculi: Initial in vitro and clinical experience," *Investigative radiology*, vol. 43, no. 2, pp. 112–119, 2008.
- [10] D. T. Boll, N. A. Patil, E. K. Paulson, E. M. Merkle, W. N. Simmons, S. A. Pierre, and G. M. Preminger, "Renal stone assessment with dual-energy multidetector CT and advanced postprocessing techniques: Improved characterization of renal stone composition—pilot study," *Radiology*, vol. 250, no. 3, pp. 813–820, 2009.
- [11] A. C. Silva, B. G. Morse, A. K. Hara, R. G. Paden, N. Hongo, and W. Pavlicek, "Dual-energy (spectral) CT: Applications in abdominal imaging," *Radiographics*, vol. 31, no. 4, pp. 1031–1046, 2011.
- [12] C. H. McCollough, S. Leng, L. Yu, and J. G. Fletcher, "Dual-and multi-energy CT: Principles, technical approaches, and clinical applications," *Radiology*, vol. 276, no. 3, pp. 637–653, 2015.
- [13] Y. Long and J. A. Fessler, "Multi-material decomposition using statistical image reconstruction for spectral CT," *IEEE transactions on medical imaging*, vol. 33, no. 8, pp. 1614–1626, 2014.
- [14] C. Mory, B. Sixou, S. Si-Mohamed, L. Bousset, and S. Rit, "Comparison of five one-step reconstruction algorithms for spectral CT," working paper or preprint, Apr. 2018. [Online]. Available: <https://hal.science/hal-01760845>.
- [15] W. Wu, P. Chen, S. Wang, V. Vardhanabhuti, F. Liu, and H. Yu, "Image-domain material decomposition for spectral CT using a generalized dictionary learning," *IEEE Transactions on Radiation and Plasma Medical Sciences*, vol. 5, no. 4, pp. 537–547, 2021. DOI: 10.1109/TRPMS.2020.2997880.
- [16] J. F. P. J. Abascal, N. Ducros, V. Pronina, S. Rit, P.-A. Rodesch, T. Brussaoud, S. Bussod, P. Douek, A. Hauptmann, S. Arridge, and F. Peyrin, "Material Decomposition in Spectral CT using deep learning: A Sim2Real transfer approach," *IEEE Access*, vol. 9, pp. 25 632–25 647, 2021. DOI: 10.1109/ACCESS.2021.3056150. [Online]. Available: <https://hal.science/hal-02952707>.
- [17] N. Ducros, J. F. P. J. Abascal, B. Sixou, S. Rit, and F. Peyrin, "Regularization of Nonlinear Decomposition of Spectral X-ray Projection Images," *Medical Physics*, vol. 44, no. 9, e174–e187, 2017. DOI: 10.1002/mp.12283. [Online]. Available: <https://hal.science/hal-01391538>.
- [18] Y. Xu, B. Yan, J. Zhang, J. Chen, L. Zeng, and L. Wang, "Image decomposition algorithm for dual-energy computed tomography via fully convolutional network," *Computational and Mathematical Methods in Medicine*, vol. 2018, no. 1, p. 2527516, 2018. DOI: <https://doi.org/10.1155/2018/2527516>.
- [19] J. Ho, A. Jain, and P. Abbeel, "Denosing diffusion probabilistic models," *Advances in neural information processing systems*, 2020. arXiv: 2006.11239.
- [20] Y. Song and S. Ermon, "Generative modeling by estimating gradients of the data distribution," in *Advances in Neural Information Processing Systems*, H. Wallach, H. Larochelle, A. Beygelzimer, F. d'Alché-Buc, E. Fox, and R. Garnett, Eds., vol. 32, Curran Associates, Inc., 2019.
- [21] Y. Song, J. Sohl-Dickstein, D. P. Kingma, A. Kumar, S. Ermon, and B. Poole, "Score-based generative modeling through stochastic differential equations," in *International Conference on Learning Representations*, 2021.
- [22] S. Arridge, P. Maass, O. Öktem, and C.-B. Schönlieb, "Solving inverse problems using data-driven models," *Acta Numerica*, vol. 28, pp. 1–174, 2019.
- [23] X. Chen, W. Xia, Z. Yang, H. Chen, Y. Liu, J. Zhou, Z. Wang, Y. Chen, B. Wen, and Y. Zhang, "SOUL-net: A sparse and low-rank unrolling network for spectral CT image reconstruction," *IEEE Transactions on Neural Networks and Learning Systems*, 2023.
- [24] Z. Wang, A. Bousse, F. Vermet, F. Froment, B. Vedel, A. Perelli, J.-P. Tasu, and D. Visvikis, "Uconnect: Synergistic spectral CT reconstruction with U-Nets connecting the energy bins," *IEEE Transactions on Radiation and Plasma Medical Sciences*, vol. 8, no. 2, pp. 222–233, 2024. DOI: 10.1109/TRPMS.2023.3330045. [Online]. Available: <https://arxiv.org/abs/2311.00666>.
- [25] Y. Song, L. Shen, L. Xing, and S. Ermon, "Solving inverse problems in medical imaging with score-based generative models," in *International Conference on Learning Representations*, 2022.
- [26] H. Chung, B. Sim, D. Ryu, and J. C. Ye, "Improving diffusion models for inverse problems using manifold constraints," *Advances in Neural Information Processing Systems (NeurIPS)*, 2022.
- [27] G. V. Cardoso, Y. J. El Idrissi, S. Le Corff, and E. Moulines, "Monte carlo guided diffusion for bayesian linear inverse problems," in *ICLR International Conference on Learning Representations*, 2024.
- [28] H. Chung, J. Kim, M. T. Mccann, M. L. Klasky, and J. C. Ye, "Diffusion posterior sampling for general noisy inverse problems," in *The Eleventh International Conference on Learning Representations*, 2023.
- [29] G. Webber and A. J. Reader, "Diffusion models for medical image reconstruction," *BJR—Artificial Intelligence*, vol. 1, no. 1, 2024.
- [30] C. Vazia, A. Bousse, B. Vedel, F. Vermet, Z. Wang, T. Dassow, J.-P. Tasu, D. Visvikis, and J. Froment, "Diffusion posterior sampling for synergistic reconstruction in spectral computed tomography," in *2024 IEEE 21st international symposium on biomedical imaging (ISBI 2024)*, IEEE, 2024. [Online]. Available: <https://arxiv.org/abs/2403.06308>.

- [31] X. Jiang, G. J. Gang, and J. W. Stayman, "Multi-material decomposition using spectral diffusion posterior sampling," *IEEE Transactions on Biomedical Engineering*, 2025.
- [32] C. Vazia, A. Bousse, J. Froment, B. Vedel, F. Vermet, Z. Wang, T. Dassow, J.-P. Tasu, and D. Visvikis, "Spectral CT two-step and one-step material decomposition using diffusion posterior sampling," in *arXiv preprint arXiv:2403.10183*, 2024. [Online]. Available: <https://arxiv.org/abs/2403.10183>.
- [33] E. Cueva, A. Meaney, S. Siltanen, and M. J. Ehrhardt, "Synergistic multi-spectral CT reconstruction with directional total variation," *Philosophical Transactions of the Royal Society A: Mathematical, Physical and Engineering Sciences*, vol. 379, no. 2204, p. 20200198, 2021. DOI: 10.1098/rsta.2020.0198.
- [34] Y. Zhang, X. Mou, G. Wang, and H. Yu, "Tensor-based dictionary learning for spectral CT reconstruction," *IEEE transactions on medical imaging*, vol. 36, no. 1, pp. 142–154, 2016.
- [35] C. Zhu, R. H. Byrd, P. Lu, and J. Nocedal, "Algorithm 778: L-bfgs-b: Fortran subroutines for large-scale bound-constrained optimization," *ACM Transactions on mathematical software (TOMS)*, vol. 23, no. 4, pp. 550–560, 1997.
- [36] R. H. Byrd, P. Lu, J. Nocedal, and C. Zhu, "A limited memory algorithm for bound constrained optimization," *SIAM Journal on scientific computing*, vol. 16, no. 5, pp. 1190–1208, 1995.
- [37] K. Mechlem, S. Ehn, T. Sellerer, E. Braig, D. Münzel, F. Pfeiffer, and P. B. Noël, "Joint statistical iterative material image reconstruction for spectral computed tomography using a semi-empirical forward model," *IEEE transactions on medical imaging*, vol. 37, no. 1, pp. 68–80, 2017.
- [38] M. Dontas, Y. He, N. Murata, Y. Mitsufuji, J. Z. Kolter, and R. Salakhutdinov, "Blind inverse problem solving made easy by text-to-image latent diffusion," *arXiv preprint arXiv:2412.00557*, 2024.
- [39] A. De Paepe, A. Bousse, C. Phung-Ngoc, and D. Visvikis, "Solving blind inverse problems: Adaptive diffusion models for motion-corrected sparse-view 4DCT," *arXiv preprint arXiv:2501.12249*, 2025.
- [40] I. Elbakri and J. Fessler, "Statistical image reconstruction for polyenergetic X-ray computed tomography," *IEEE Transactions on Medical Imaging*, vol. 21, no. 2, pp. 89–99, 2002. DOI: 10.1109/42.993128.
- [41] P. J. Huber and E. M. Ronchetti, *Robust statistics*. John Wiley & Sons, 2011.
- [42] X. Jiang, S. Li, P. Teng, G. Gang, and J. W. Stayman, "Strategies for CT reconstruction using diffusion posterior sampling with a nonlinear model," *ArXiv*, arXiv:2407, 2024.
- [43] M. Ronchetti, "Torchradon: Fast differentiable routines for computed tomography," *arXiv preprint arXiv:2009.14788*, 2020. eprint: arXiv:2009.14788.
- [44] M. Li, M. Wu, J. Pack, P. Wu, B. D. Man, A. Wang, K. Nieman, and G. Wang, *Coronary atherosclerotic plaque characterization with photon-counting CT: A simulation-based feasibility study*, 2023. arXiv: 2312.01566 [physics.med-ph]. [Online]. Available: <https://arxiv.org/abs/2312.01566>.
- [45] R. Zhang, P. Isola, A. A. Efros, E. Shechtman, and O. Wang, "The unreasonable effectiveness of deep features as a perceptual metric," in *CVPR*, 2018.
- [46] J. Punnoose, J. Xu, A. Sisniega, W. Zbijewski, and J. Siewerdsen, "Spektr 3.0—a computational tool for x-ray spectrum modeling and analysis," *Medical physics*, vol. 43, no. 8Part1, pp. 4711–4717, 2016.
- [47] S.-M. Latva-Äijö, F. Zanetti, A.-P. Honkanen, S. Huotari, J. Gondzio, M. Lassas, and S. Siltanen, "Inner product regularized multi-energy x-ray tomography for material decomposition," *Applied Mathematics for Modern Challenges*, vol. 2, no. 1, pp. 1–16, 2024, ISSN: 2994-7669. DOI: 10.3934/ammc.2024001. [Online]. Available: <http://dx.doi.org/10.3934/ammc.2024001>.
- [48] A. Chambolle and T. Pock, "A first-order primal-dual algorithm for convex problems with applications to imaging," *Journal of mathematical imaging and vision*, vol. 40, pp. 120–145, 2011.
- [49] S. Boyd, N. Parikh, E. Chu, B. Peleato, J. Eckstein, et al., "Distributed optimization and statistical learning via the alternating direction method of multipliers," *Foundations and Trends® in Machine learning*, vol. 3, no. 1, pp. 1–122, 2011.
- [50] F. Guth, S. Coste, V. De Bortoli, and S. Mallat, "Wavelet score-based generative modeling," *Advances in neural information processing systems*, vol. 35, pp. 478–491, 2022.
- [51] P. Friedrich, J. Wolleb, F. Bieder, A. Durrer, and P. C. Cattin, "WDM: 3D wavelet diffusion models for high-resolution medical image synthesis," in *MICCAI Workshop on Deep Generative Models*, Springer, 2024, pp. 11–21.
- [52] C. Phung-Ngoc, A. Bousse, A. De Paepe, H.-P. Dang, O. Saut, and D. Visvikis, "Joint reconstruction of activity and attenuation in PET by diffusion posterior sampling in wavelet coefficient space," *arXiv preprint arXiv:2505.18782*, 2025. [Online]. Available: <https://arxiv.org/abs/2505.18782>.
- [53] A. De Paepe, A. Bousse, C. Phung-Ngoc, Y. Mellak, and D. Visvikis, "Adaptive diffusion models for motion-corrected cone-beam head CT," *arXiv preprint arXiv:2504.14033*, 2025. [Online]. Available: <https://arxiv.org/abs/2504.14033>.
- [54] J. Ho, C. Saharia, W. Chan, D. J. Fleet, M. Norouzi, and T. Salimans, "Cascaded diffusion models for high fidelity image generation," *Journal of Machine Learning Research*, vol. 23, no. 47, pp. 1–33, 2022.
- [55] V. De Bortoli, J. Thornton, J. Heng, and A. Doucet, "Diffusion schrödinger bridge with applications to score-based generative modeling," *Advances in Neural Information Processing Systems*, vol. 34, pp. 17695–17709, 2021.
- [56] J. Song, C. Meng, and S. Ermon, "Denoising diffusion implicit models," *arXiv preprint arXiv:2010.02502*, 2020.
- [57] R. Barbano, A. Denker, H. Chung, T. H. Roh, S. Arridge, P. Maass, B. Jin, and J. C. Ye, "Steerable Conditional Diffusion for Out-of-Distribution Adaptation in Medical Image Reconstruction," *IEEE Transactions on Medical Imaging*, vol. PP, pp. 1–1, Jan. 2025. DOI: 10.1109/TMI.2024.3524797.